STRUCTURE AND KINEMATICS OF A JET-ACCRETION DISK SYSTEM

L. CANO-FERNANDEZ[1†] & G.N. ORTÍZ LEÓN[2]

[1]Universidad Mayor de San Andrés, La Paz-Bolivia.
[2]Instituto Nacional de Astrofísica, Óptica y Electrónica, Puebla-México

ABSTRACT

We present a study of two Young Stellar Objects (class 0-I): CARMA 6 and CARMA 7, using observational data from the Very Long Baseline Array (made between 2020 and 2022), this array have a great angular resolution of the order of $10^{-4}[arcsec]$. We searched for water maser emission at 22.23508GHz and investigated their spatial distribution. Using the Doppler effect we recognized velocity structures that trace the kinematics of the disk. Our results provide new evidence that supports the disk-wind model as a mechanism for the star to get rid of angular momentum in the accretion disk and eject protostellar jets. For CARMA 6 we got launching radios around $6[AU]$ that are consistent with the model. On the other hand, we couldn't find enough sources around CARMA 7 to replicate the same calculations.

Subject headings: Stellar Astrophysics, Radio Astronomy, Young Stars Objects

1. INTRODUCTION

As a star goes through its different evolutionary stages, it undergoes different processes (physical, chemical) that lead to determining various characteristics of it, for example, the initial mass with which the star is made up is a great determinant at the moment. to know what your final destination will be. Thus, in the area of stellar evolution, each stage can be studied extensively. This project seeks to focus on relatively young stars (between 100000 and 1 million years old), which are called young stars or in the protostellar phase.

1.1. *Evolutionary stages*

Stars form in regions where there is abundant stellar dust and cold gas, where a core is formed that, by collapse, becomes a protostar, which is called stage 0 (Dunham et al. (2014)), later the material around the new star begins to be accreted and finally the star passes to a stage I. In a common notation, to refer to a young star the acronym (YSO) is used, which comes from Young Stellar Object

1.2. *Stages and classes*

In the review by Dunham et al. (2014), a clear distinction is made between class and stage, where the use of the term stage is proposed when it refers to the evolutionary state of the star and class when it refers to their observations and classification.

When the star is still very young, the dust around it makes it impossible to observe it in bands such as optical, and for stars up to a limit of 500 pc, they are better observed in infrared wavelengths such as Spitzer and Hershel. The explicit definition of classes I, II and III is strongly related to the infrared spectral index, while class 0, being best observed submil-

limeterly, is defined as the radius between the light luminosity measurements and the bolometric luminosity.

1.3. *Protostellar disks and jets*

As also seen in the figure 1, in the early stages of evolution, the star has an associated disk and jet, the disk contributes to the accretion of the material, while the jet is a way for the star to free itself from the moment angular. We will focus on low mass stars when possible.

1.3.1. *Jets*

Lee (2020) proposes that an important way to observe molecular jets is through submillimeter wavelengths, specifically the CO, SiO and SO lines. A great advantage is that the molecular lines are not affected by extinction due to the dust found around the YSO, so observing these molecular lines allows us to observe very close to the star and also study: the accretion process, formation of a possible binary system, even the formation of planets in the disk.

Specifically, the jets come from a magneto-centrifugal force from the nearest section of the disk, so it would be normal to expect them to be rotating, so angular momentum can be extracted thanks to the jets, which would allow the material in the disk to be really get to the young star. In the current literature, there is little observational evidence of this magneto-centrifugal mechanism, one of this evidence is the work carried out by Moscadelli et al. (2022), which focuses on studying the behavior of water masers in an intermediate mass star. (compared to this work that focuses on low mass stars), which also has resolutions of some AU.

Something important when observing molecular jets is to have an acceptable inclination, that is, the jet is not affected by projections in its direction. Another requirement is angular resolution, since the
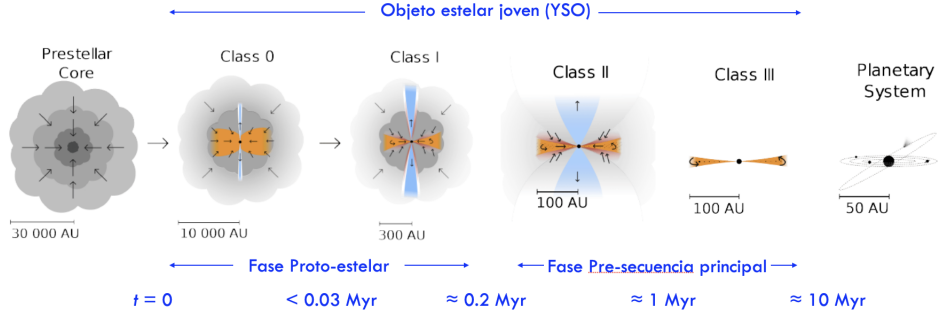
---

†Email: lcanof@fcpn.edu.bo

Caso estrellas de baja masa ($\lesssim 2\ M_{Sol}$)

FIG. 1.— Stages of evolution of a YSO. This project is focused in classes 0 and I. Figure adapted from M. Persson on Figshare

origin of jets is currently thought to occur at AU scales. This is only achievable through the use of interferometers. Furthermore, it is desirable to have speed resolutions less than 1 kilometer per second to be able to study narrow emission

1.3.2. *Disks*

According to Dunham et al. (2014), a rotating Keplerian structure is defined and named as a disk, and must have been formed during the early evolution of the protostar. Each disk brings with it an amount of angular momentum, which can be caused by an initial rotation of the cloud of material or by turbulence in the medium around the new star. An important aspect of the disk is that it allows the only way to directly determine the mass of the protostar, since it is deeply embedded in its dust, preventing its spectral measurement. Again, with interferometers such as the Very Large Array (VLA), Very Long Baseline Array (VLBA), and Atacama Large Millimeter/submillimeter Array (ALMA), the improved angular resolution can help with the determination of new, or even new, protostellar masses. and improved disc measurements.

1.4. *Astrophysical Masers*

Much like atoms, molecules also have energy levels due to various modes of vibration, rotation or movement. Gray (1999) explains that if a greater number of molecules are found at higher energy levels than at a lower level, there is a population inversion , which is a fundamental requirement for the origin of masers. Once a photon interacts with these molecules, stimulated emission occurs and masers are created (*microwave amplification by stimulated emission of radiation*). A definition very close to lasers, in a very simplified way we can think of a maser as a microwave laser .

Although astrophysical masers were detected approximately 60 years ago, they have become a very important way to study phenomena that were not well understood. Some of the first lines to be discovered were the OH (hydroxide) molecule, H2O, SiO and CH3OH, so we can notice that they can go from atomic states of hydrogen to complex molecules such as methanol, taking into account that Each molecule

can have several transitions, the complete list of masers is quite extensive and they can be measured in different ranges of the electromagnetic spectrum.

In addition to a list of which masers exist, the list of the sources that originate them is a large area, the most common being areas of star formation, envelopes of already formed stars, supernova remnants and even comets within our solar system (Gray (1999)).

Speaking of the size of these emissions, a maser can have angular sizes of milli arc seconds (more) or even less, which if we convert to physical units for sources within the Milky Way, a few astronomical units (AU) are equivalent. Therein lies the importance of having good angular resolution, which will be explained with the use of interferometry. As masers are almost always small (relative to their environment), that is, compact with respect to the environment in which they are located, this makes them a diagnostic tool for their environment. Finally, the shape is not completely defined either, since source maps show irregular shapes.

In this project we will focus on the structure and kinematics of the water masers (described below), while continuing to rely on the SiO line that is used as a jet tracer (Podio et al. (2021)).

1.4.1. *Water masers*

Focusing a little on the objective of this project, the line of water masers is studied in the environment of a young star (YSO), according to Gray (1999) the YSO injects energy into the interstellar medium through shock waves, and If these waves are not powerful enough to dissociate the water, they will generate the energy to be the driver of a population inversion. This is taken advantage of because the main characteristic of the masers close to a YSO is their brightness, which can be more powerful than that of the Sun.

As mentioned above, molecules can emit masers in different transitions, in this case they can range from 22 GHz to 658 GHz. In the case of the water molecule, the brightest maser transition occurs at 22.23508 GHz.

1.5. *Radio Interferometry*

1.5.1. *Radioastronomy*

The study of astronomical objects and phenomena was for many centuries restricted to the visible band. When humanity developed new technologies and tools, these measurements expanded their spectrum. An important event is the measurement carried out by Jansky in 1931, demonstrating that radiation originating outside the planet was observed, with a wavelength of 20.5 MHz. In the literature by Wilson et al. (2016), it is defined that the radio window goes from wavelengths of 10 -15 meters to lengths of 0.3 mm. In order not to make this short introduction too long, it is worth clarifying that although the objects studied in the visible window are normally measured by their thermal radiation, in radio astronomy the phenomena are not always like this, giving the possibility of studying other physical mechanisms.

In radio astronomy it is common to use the Jansky per steradian (Jy sr-1) or Jy per telescope beam to measure the specific intensity of a maser. The Jy being a measure of flux density $(10^{-26}Wm^{-2}Hz^{-1})$. Subsequently, it is common to convert the spectral frequencies to velocity spectral lines using the Doppler effect; this step is very relevant and will be better developed in the methodology. Jansky's definition is:

$$1Jy = 10^{-26}\frac{W}{Hz \cdot m^{-2}} = 10^{-23}\frac{erg}{s \cdot Hz \cdot cm^{-2}}$$

1.5.2. *Angular resolution*

Remembering the common definition of angular resolution (θ) as the ability to distinguish (or resolve) two objects separated at that angular distance, we can use the equation:

$$\theta = \lambda k/D \tag{1}$$

where λ is the wavelength, D the diameter of the instrument and k is a constant derived in Wilson et al. (2016). Now, if we talk about radio wavelengths, as described in the previous section, these are relatively large, on the order of millimeters to meters, so to obtain a good angular resolution (the objective is to minimize the value) we should compensate for it with a very large instrument diameter. Then one finds the limit of materials to create a huge telescope, which according to the same author, reaches 300m.

To solve this problem, an interferometer proposed by Michelson is used, which can have an angular resolution of $\theta \approx \lambda/D$ two instruments with a diameter d that are separated by a distance D are used when $D \gg d$. We are facing the emergence of interferometers the size of countries or even a good section of the earth (such as the Event Horizon Telescope or EHT).

1.5.3. *Basic interferometers*

Now we must work on how the signal received by both instruments should be treated for our purposes. The operation of an interferometer is based on the
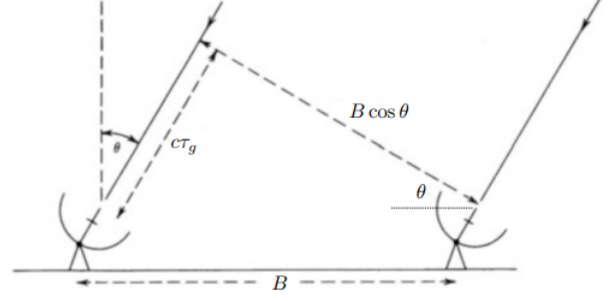

FIG. 2.— Array of two antennas, separated by a distance B. Figure adapted from Thompson et al. (2017)

principle of interference, where if two electromagnetic waves overlap, they can interfere with each other, increasing or decreasing their amplitude. In the case of telescope arrays, the captured signals are combined in a correlator, which precisely measures the correlation between these signals.

We start with a simple arrangement of two antennas, which are separated by a distance B, and pointing at a zenith angle θ, as seen in figure 2.

For a point source, the signal will arrive at antenna 2 (left in figure 2) with a slight delay, which is geometrically related to the distance that separates both antennas and at the same time to the zenith angle at which they are observing, which is how we define a geometric delay (τ_g) that has the form:

$$\tau_g = \frac{B\sin\theta}{C} \tag{2}$$

Now we focus on the signal that both antennas receive, this will be given by R_1 and R_2 respectively:

$$R_1(t) = E\sin(2\pi\nu t) \tag{3}$$
$$R_2(t) = E\sin(2\pi\nu(t - \tau_g)) \tag{4}$$

Subsequently, this signal is multiplied and integrated over time (the correlator takes care of this):

$$R_{12}(t) = E^2\sin(2\pi\nu t)\sin(2\pi\nu(t - \tau_g)) \tag{5}$$

Which is then integrated and we get

$$\frac{1}{T}\int_0^T R_{12}(t)dt \tag{6}$$

However, now a signal delay from antenna 2 is created instrumentally, which will be shifted by 90 degrees. This helps us make the signal complementary (between sine and cosine), thus preventing the telescope from being "blind" at certain angles, generating an "imaginary" response:

$$R_{12}(t) = \frac{1}{2}E^2\sin(2\pi\nu\tau_g) \tag{7}$$

Using complex representations, we can put together the relationship

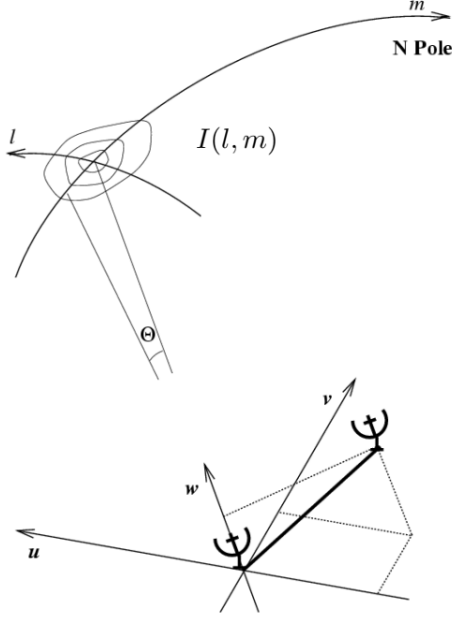$$C_{12}(t) = \frac{1}{2}E^2\cos(2\pi\nu t) + \frac{1}{2}E^2\sin(2\pi\nu t) \tag{8}$$

FIG. 3.— Sky plane (top), and Fourier plane (bottom)

Doing the variable changes of $u = B/\lambda$ and supposing $\operatorname{sen} \theta \approx \theta = l$ the expression becomes

$$C_{12} = \frac{1}{2}E^2 e^{2\pi i u l} \qquad (9)$$

For an extended source the situation is complicated, since we must integrate into a space that will be called "sky plane". The previous expression corresponds to the result of the correlation of the signals coming from a single point (which if we place it in the plane of the sky will have a coordinate l). The next step is to consider the extent of the celestial object along this coordinate and then its extent in two dimensions (l, m). If we look for visibility again, it will be to integrate the signal in a given coordinate and project it in another (Fourier plane or complex plane). Schematically we can see in figure 3 the relationship between the two coordinate systems (l,m) $\rightarrow$ (u,v).

Integrating the expression for a point source, C_{12}, we arrive at a relationship of the form,

$$V(u) = \int_{-\infty}^{\infty} I(l) e^{2\pi u l} dl \qquad (10)$$

where $I = E^2/2$, is the Stokes relation that will be called *sky brightness* and $V(u)$ is the visibility at a point u. At the same time we can see that if we do an inverse Fourier transform, we obtain the brightness again, that is, we can conclude that these two magnitudes are related by a Fourier Transform.

$$I(l) = \int_{-\infty}^{\infty} V(u) e^{-2\pi u l} dl \qquad (11)$$

Now, these relations were valid in only one coordinate (u or l), but if we go to the general case we
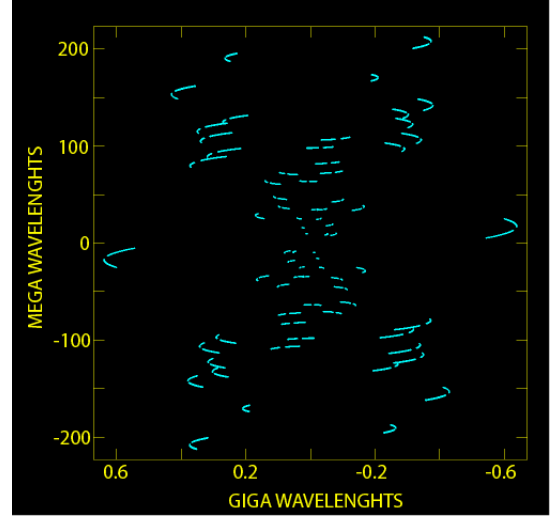

FIG. 4.— UV Coverage plane (visibilities) for epoch E of CARMA 6

need a double integral, that is, the transform and its inverse will be:

$$V(u,v) = \int_{-\infty}^{\infty} \int_{-\infty}^{\infty} I(l,m) e^{2\pi(ul+vm)} dl dm \qquad (12)$$

$$I(l,m) = \int_{-\infty}^{\infty} \int_{-\infty}^{\infty} V(u,v) e^{-2\pi(ul+vm)} du dv \qquad (13)$$

Thus, we can have visibility between a pair of antennas V_{ij}, and these visibilities live in the Fourier plane, where the coordinates are u and v, and are measured in giga or mega wavelengths.

Finally, it is worth mentioning that since visibilities are complex numbers, they can be expressed in terms of a phase and an amplitude, that is:

$$V_{ij} = |V_{ij}| e^{i\phi_{ij}} \qquad (14)$$

We are particularly concerned about this phase ϕ, as it is a fundamental part of data calibration. An example is the one obtained during data calibration (which will be explained in the methodology). An example of a visibilities map is seen in figure 4.

1.5.4. *Disk wind*

According to the theory described in Lee (2020), protostellar jets serve to extract angular momentum from the innermost regions of the disk, allowing material to be accreted toward the star. But there must also be other mechanisms that serve to remove angular momentum from the disk, one that is widely studied is the disk model, in which the material close to the star (around 20 astronomical units) is ejected from an extended disk (thus removing the angular momentum), throwing this material towards the outside of the disk.

1.5.5. *The Very Long Baseline Array (VLBA)*

It is the arrangement from which the data for this degree project was obtained, according to NRAO , it consists of 10 telescopes distributed throughout the

United States, the maximum separation between antennas is 8611 km, which results in an angular resolution between 0.17 and 22 milli arcseconds (mas). The 10 telescopes are:

1. St. Croix – US Virgin Islands

2. Hancock–New Hampshire

3. North Liberty–Iowa

4. Fort Davis – Texas

5. Los Alamos – New Mexico

6. Pie Town – New Mexico

7. Kitt Peak – Arizona

8. Owens Valley – California

9. Brewster–Washington

10. Mauna Kea – Hawaii

2. METHODS

2.1. *Data used*

For this project, observations from the Very Long Baseline Array (PI: G. Ortiz-León) were used, which took place between 2020 and 2022. These data are separated by epochs, where each epoch is an observation separated approximately by one month from each other, 1 shows the epochs, Julian day (and its conversion to date), angular resolution, spectral resolution and the RMS noise measurement (*root mean square*), which is the square root of the square mean, which is used as a noise measure, this was averaged over all the channels used.

It should be noted that epochs G and H are also available for CARMA 6, however, they were not used because the masers are practically not visible, so they will not support the necessary calculations. The table shows the `VLA_OBS` observation, which is a complementary observation with the Karl G. Jansky Very Large Array (VLA), another radio interferometer, which was used to have an observation of the star's own position, this observation only has a channel, since these are observations of the continuum (emission of a wide range of frequencies).

Epochs D, E and A5 were calibrated from scratch as part of the learning process for this degree project, the other epochs were analyzed directly from a calibrated cube. Below is an overview of the calibration process of this data to obtain a cube and subsequently analyze it with CASA.

2.2. *VLBA Data Calibration*

The software *Astronomical Image Processing System* (AIPS) was used, this program is focused on radio astronomy widely used for data calibration, data analysis and other necessary tasks with astronomical data. It is currently hosted on the website of the National Radio Astronomy Observatory (NRAO), it is a relatively old package (being used since around 1980), but still very relevant, having support and additions such as its connection with Python.

AIPS is a software that is based on *tasks*, each one can be thought of as a function that takes certain parameters and makes the necessary changes or calculations. One can do a series of tasks to perform data calibration.

The calibration process consists not only of correlating the data as explained in the introduction, but also of making corrections due to different factors that may affect the measurement, such as geographical variations (high measurement precision is needed between antennas), where we must correct possible errors in the positions of the different antennas on the ground, and other instrumental errors that deteriorate the data. Other factors that cannot be controlled, for example, would be clouds over some of the antennas, which would delay the signal more than expected.

In itself, the visibility measured by the antennas is affected by "gains", which are complex numbers and are multiplied by the real visibility, so we can think about the relationship:

$$\hat{V}_{ij}(t) = g_i(t)g_j^*(t)V_{ij} \quad (15)$$

Where $\hat{V}_{ij}(t)$ is the observed visibility, V_{ij} is the actual (or real) visibility, while $g_i(t)$ and $g_j^*(t)$ are the gains that affect the visibility.

So, to correct the data, correction tables of the form g_i^{-1} must be applied to obtain the final correction. This process is carried out several times, with some correction tables obtained from the data that we already have, or some coming from external data, a diagram of how it works is found in figure 5.

Now, remembering that when we were talking about the signal received by two antennas there will be a delay, this can be related to a relative phase between the fields measured by separate antennas, the delay can also be affected by the atmosphere, electronics or the ionosphere, reaching a total delay ($\Delta\tau$), also affecting the phase measured by the correlator, that is, we will have a phase error $\Delta\phi$.

The phase generated by a correlator will then have the form:

$$\phi_{corr}(t,\nu) = \phi_V(t,\nu) + \phi_{inst}(t,\nu) + \phi_{geom}(t,\nu) \\ + \phi_{atmo}(t,\nu) + \phi_{iono}(t,\nu) \quad (16)$$

Where the meaning of each phase is:

- ϕ_{corr} generated by the correlator

- ϕ_V True visibility

- ϕ_{inst} instrumental phase error

- ϕ_{geom} geometry error

- ϕ_{atmo} and ϕ_{iono} are error due to neutral atmosphere and the ionosphere

TABLE 1
Observing epochs, corresponding dates and resolutions.

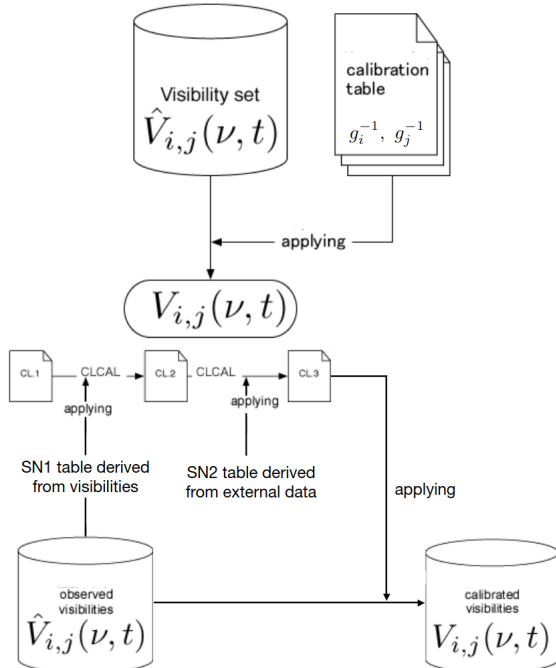| Epoch	JD	Date	Angular res [arcsec]	Spectral Res [Hz]	RMS
CARMA6_A4	2459148,473	2020-10-25	6.6E-4	1.56E4	2.7E-2
CARMA6_A5	2459307,043	2021-04-02	7.4E-4	1.56E4	3.7E-2
CARMA6_A	2459653,083	2022-03-14	7.6E-4	1.56E4	2.3E-2
CARMA6_B	2459681,007	2022-04-11	9.2E-4	1.56E4	2.0E-2
CARMA6_C	2459705,938	2022-05-06	7.1E-4	1.56E4	2.4E-2
CARMA6_D	2459729,873	2022-05-30	8.2E-4	1.56E4	1.7E-2
CARMA6_E	2459738,845	2022-06-08	7.6E-4	1.56E4	1.9E-2
CARMA6_F	2459767,769	2022-07-07	7.1E-4	1.56E4	1.7E-2
VLA_OBS	2459771,750	2023-07-11	5.63E-2	1.56E4	1.7E-2
CARMA7_A	2459652,413	2022-03-14	0.24E-4	1.56E4	1.1E-2
CARMA7_B	2459680,512	2022-04-11	9.23E-4	1.56E4	0.8E-2
CARMA7_C	2459705,356	2022-05-06	7.08E-4	1.56E4	1.3E-2

Fig. 5.— Schematic of the general calibration process (up) and the detailed process (right). Figure created by Seiji Kameno (private communication)

Although the effects, origins and solutions to each of the errors presented can be discussed in detail, this is outside the scope of this article. The important thing to highlight is that these phase errors will be corrected in the calibration process to have a correct signal. To help us with the calibration, a code called ParselTongue was used, which we will describe below.

2.3. *ParselTongue*

ParselTongue (Kettenis et al. (2006)) is an integration of AIPS with Python, in this case we will use data reduction from BeSSel (The Bar and Spiral Structure Legacy Survey) which, in addition to the article by Reid et al. (2014), is commonly used in interferometer data, and as a basis we have the guide by Andreas Brunthaler[1]. The advantage is that it is an interactive process that summarizes the

[1] Provided by private communication

steps for data calibration. To run it you need to meet the Python version requirements and have AIPS installed.

Thus, in a common calibration process of data obtained with the VLBA, 3 files are needed for each calibration, which will be entered in the code used:

- OBJECT.CONT.idifits: Continuous data obtained by the antennas

- OBJECT.LINE.idifits: Desired line data (spectral zoom) obtained by the antennas

- OBJECT.GEO.idifits: Geographic data from all-sky gauges (also known as geodetic gauges in the specialized literature).

Where OBJECT is the time or some name referring to the observation made.

Subsequently, several of the parameters are to control the behavior of the code, as we seek to have intervention in some of the steps, we will use the interactive version, which shows graphics to help in the calibration process. In addition to using a calibration source, which is a bright and compact astronomical object (usually a quasar) to improve the quality of the data obtained in the end.

As an example we will use calibration by instrumentation, the objective is for the phase to change smoothly (increasing or decreasing) over time and also between the antennas. For example, we can see the before and after of this step in figure 6.

2.4. *CASA*

CASA (Common Astronomy Software Applications) is a software developed by the NRAO, in it we can perform several tasks that will be very useful in the analysis process, it is only available on Linux and MacOS operating systems. For this, we must first be very clear about the structure and language that we will use to manage the data.

An epoch consists of a data cube, a cube can be understood very literally since it is a structure of 3 variables, a referential form can be seen in figure 7. To refer to the different wavelengths (or frequencies) available for the cube we will use the channels, where we will have a specific amount determined by
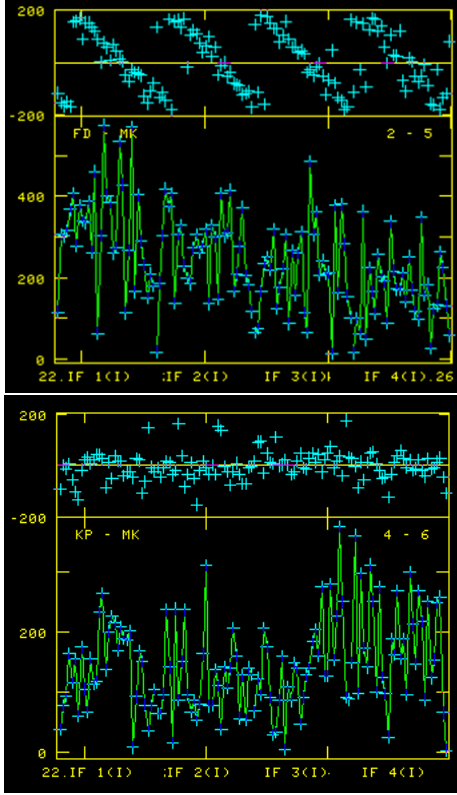
FIG. 6.— Instrumental calibration, before calibration (up) and after calibration (bottom), between the Fort Davis (TX), KP (Kitt Peak, AZ) and Mauna Kea (HI) antennas
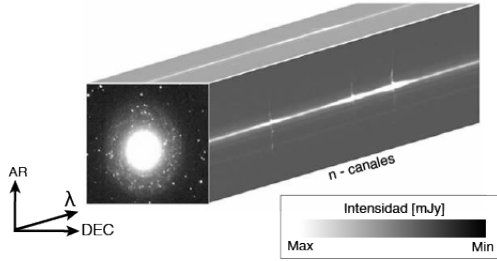

FIG. 7.— Structure of a data cube, on the wavelenght axis (λ) we can also relate a frequency (ν), or speed through the Doppler effect, this is explained later. Adapted from the National Astronomical Observatory of Japan.

the spectral resolution of the data (see 1). At the same time, a frequency can be related to a speed, thanks to the Doppler effect, which will be explained later. At a specific frequency, sources can be recognized through their intensity, which is measured in milli Janskys (mJy).

CASA is primarily managed by tasks that can be seen as functions or routines, since they have input parameters, the program carries out the process and one obtains results in the format of Python dictionaries or in the CASA log window. Some of the tasks that were used (and some will be described in more detail later) are:

- `imview` : Allows you to view a data cube.

- `imhead`: Gives information about the header of the data.

- `imfit` : Given a specific region and channel, fits a Gaussian distribution to obtain the peak flow and position in that region.

- `imsubimage` : Allows you to crop a data cube, either by coordinates or by channels.

- `imstats` : Calculates statistics for a specific region.

So, the first thing you do when receiving a data cube is to open it with imview, this should be something simple, however, a typical cube is usually around 12.5 GB of space, which requires a lot of computing power, this did that even the program tends to stop responding and you have to start from scratch. Thus, it was decided to cut the cube (using imsubimage) to only the channels where masers are observed and also delimit the region where they appear, this reduced the data to consisting of around 30 to 40 channels (instead of the 200 originals) and the space occupied by the file does not exceed 200MB.

2.5. *Map of sources*

Once we have the cube ready (cut out), it is opened and a contrast adjustment is made with the CASA controls. To recognize a source on a specific channel, perform the following steps:

- The cube is opened again, this time in the form of outlines. The contours are recalculated to 7, 9, 11 and 13 σ, where σ is the RMS value of a region that we know does not have a signal, this helps us ensure that the sources that we recognize are above 7 sigma, which is a robust signam.

- Subsequently, the source is enclosed in a region, this is characterized by numbers of pixels as coordinates, which will be set as parameters in the imfit task , next to the channel on which we are working.

- imfit returns the result of the adjustment as a dictionary (python), so exploring it we are left with the information of `x_rad`, `y_rad` (position of the peak in radians), `peak_flux` (peak flux in Jy/beam) and freq (frequency in Hz).

This process is done separately on all channels, and if there is more than one source on a channel the last two steps are done multiple times. To automate this a little (that is, not do step by step at CASA), a code was made that takes as parameters the channel, the box (region), and source number, then prints the results generating a table in a file of results, so one changes the parameters and the process speeds up. This is one of the great advantages of CASA, since it is easily integrated with Python.

2.6. *Corrections and discrimination of sources*

Once we have the sources from all the epochs, we must remember that (although it is minimal), the

sources will have their own movement through time, and as some are separated by several months or even years, we must correct for parallax and movement own. For this objective we will use a code provided to correct the coordinates, initially it needs the following parameters:

- Julian day of the epoch to be corrected `jd`

- Julian day of the reference epoch `jd`

- Position of the earth at the epoch to be corrected, represented by heliocentric coordinates: `earth_x`, `earth_y` and `earth_z`

- Proper movement of the star, which is constant

Subsequently, the parallax ellipse projections of RA and DEC (which are functions of time) are used and the new positions of the masers are obtained, now all at a desired epoch. These equations are well described in Loinard et al. (2007). Where we consider that the right ascension (α) and declination (δ) of a celestial body vary based on its trigonometric parallax (π) and proper motion (μ) as a function of t:

$$\alpha(t) = \alpha_0 + (\mu_\alpha \cos\delta)t + \pi f_\alpha(t) \qquad (17)$$
$$\delta(t) = \delta_0 + \mu_\delta t + \pi f_\delta(t) \qquad (18)$$

Where α_0 y δ_0 are the coordinates of the source at a reference epoch, μ_α and μ_δ the components of the proper motion and f_α y f_δ are the projections of RA and DEC of the parallactic ellipse, being defined with the barycentric position of the earth in AU as

$$f_\alpha(t) = (X\sin\alpha - Y\cos\alpha)/15\cos\delta \qquad (19)$$
$$f_\delta(t) = X\cos\alpha\sin\delta + Y\sin\alpha\sin\delta - Z\cos\delta \qquad (20)$$

Now, we must know what conditions to take into account for a maser to be considered a real source (i.e., minimize the possibility of including artifacts or possible false detections), we take two parameters:

- The maser must appear on at least 2 spectral channels on a given epoch.

- The maser must appear in at least two epochs (not necessarily consecutive).

If our source meets both conditions, we consider it a real source. Figure 8 shows how a source appears in different speed channels, where 12.5km/s approximates our resting speed (in a Doppler effect it should be the real frequency of the emission).

2.7. *New coordinate system and Doppler effect*

At this moment our sources are in the plane of the sky, but we cannot know if they have any angle with respect to the disk (or jet) of the star, for this we rely on the observations of Podio et al. (2021), to find that the star has a jet at an angle of 25 degrees measured from the north to the east. We must be careful, because this is the angle with respect to the plane of

the sky, and we do not know if the jet is also inclined towards us or towards the opposite of the plane of the sky.

With this angle we can construct a new coordinate system, where the x-axis is perpendicular to the jet. For that we use rotation formulas, which are the following:

$$R = x\cos\theta + y\sin\theta \qquad (21)$$
$$Z = -x\sin\theta + y\cos\theta \qquad (22)$$

Where R is the coordinate in the disk, Z in the jet direction, θ is the angle to rotate (taken from Podio et al. (2021)) and x and y are the current coordinates in the sky plane (by convention RA and DEC, respectively).

At the same time it is useful to know the speed at which these masers trace the disk or the jet, for that we will use the fact that the masers are measured not exactly at the frequency of the water maser (22.23508 GHz), but in channels around it. If we remember the Doppler effect, a moving object that emits at a given frequency will be perceived by an observer at another frequency, if the object approaches, a higher frequency will be observed and if the object moves away, the measured frequency will be lower. The relationship to calculate this speed (v) is:

$$v = \frac{c \cdot (\nu_0 - \nu)}{\nu} \qquad (23)$$

Where ν_0 is the resting frequency (in our case 22.23508 GHz), ν is the measured frequency (the channel where the maser was found), and c is the speed of light. Finally we must take into account the systemic speed, which is close to 12.5 km/s, by subtracting it from all the speeds obtained, we will have positive speeds (moving away), or negative speeds (approaching).

3. RESULTS

3.1. *CARMA 6*

After processing the 7 observations for CARMA 6, in addition to obtaining the position of the star through the observation with the VLA, the final map of sources can be obtained, which can be seen in figure 9. It is relevant to comment that the positions are still in arcseconds and not in units of length, since this calculation will be carried out later.

The observation with the VLA carried out in July 2023 (described in 1) gives us information on the position of the star, in this case it has equatorial coordinates $\alpha = 18h30m3.5420s$ and $\delta = -23'8.41725''$. With this we can do the coordinate transformation and the offset (calculate the distance from the center of the star, which was also corrected for parallax), thus obtaining the result seen in figure 10:

Now we must make a last filter to generate our final map, as was mentioned in the source correction and discrimination section, then we must verify that the sources are present in at least two epochs and each one in two channels per epoch, thus performs
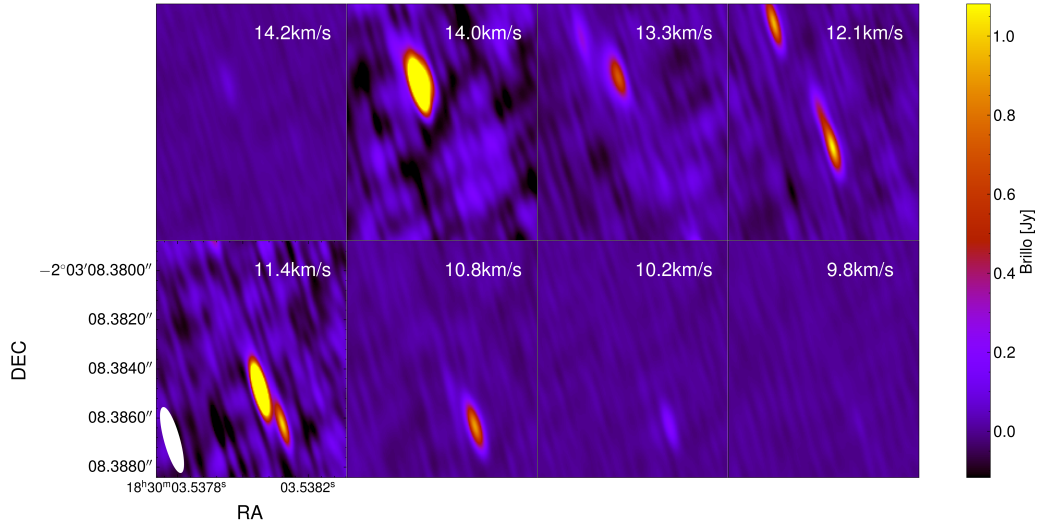
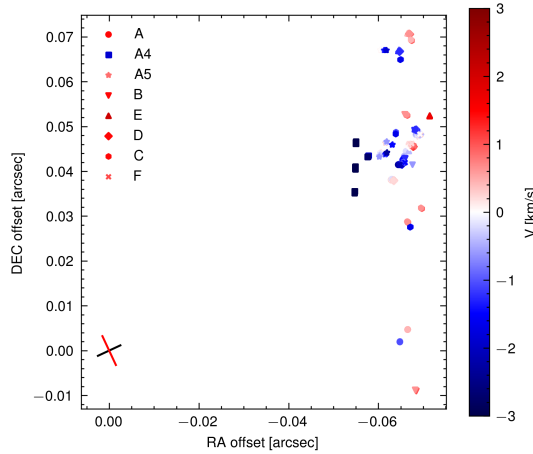FIG. 8.— Intensity map of the brightest maser seen in different velocity channels (epoch A of CARMA 6).

FIG. 9.— Map of CARMA 6 observations. Different marks denote different epochs and the color is the Doppler corrected velocity. In the lower left part the orientation of the disk and jet of the star in question is shown, whose position was obtained with the VLA and determines our origin of coordinates.
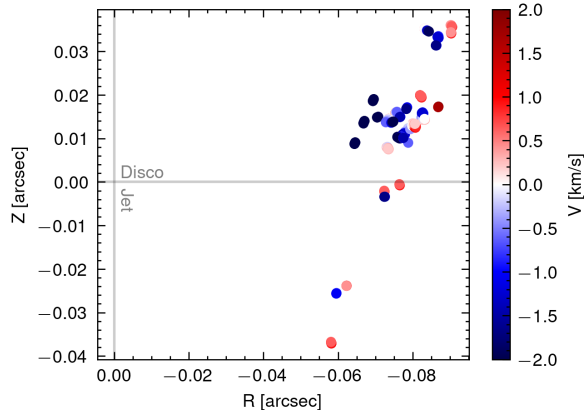

FIG. 10.— CARMA 6 masers in the new coordinate system, the plumb lines show the direction of the disk and jet. The color bar indicates the current speed.

almost manual data deletion, as seen in figure 11. It is not possible to recognize structures with the naked eye, but as a general comment we observe that the majority of the masers show a filamentary or linear distribution with a significant inclination with respect to the disk. Furthermore, they are located at a scale of approximately 30 astronomical units from the center of the star, that is, far from the jet. Given these characteristics, we can propose that these observations can be studied with the disk wind model. Under this model, the linear structures correspond to a flow of gas that is being expelled from the surface of the disk while maintaining the rotation of the gas around the star.

We are now at the point to do the rotation analyses, so it is useful to plot the radius versus velocity. To do this, a matrix is created with the distribution of all the masers, separating them by era to have a better visualization. which can be seen in figure 12. In this graph you can see some "traces", which are masers that have both a blue and a red part, some of these masers are consistent in several epochs, while others (a clear example are the masers of epoch A4) , do not have a counterpart in speed, the speed map of all epochs at the same time is seen in figure 13.

Something that will also be explained in the epoch spectra is that the masers are not constant, and we can even think that some may possibly have a semi-periodic behavior, which could be studied with future observations.

3.1.1. *Disk speed*

Now that we have a finalized map, we can see the distribution of the masers and their redshift or blueshift. We will project the masers onto the R axis of the disk, and plot the position along this axis against the velocity of the maser (figure 13). According to the rotation of a disk, we should have a velocity gradient, and if we see structures that form what look like "traces" (that is, sources that have the same slope), we will do linear regressions to obtain the an-
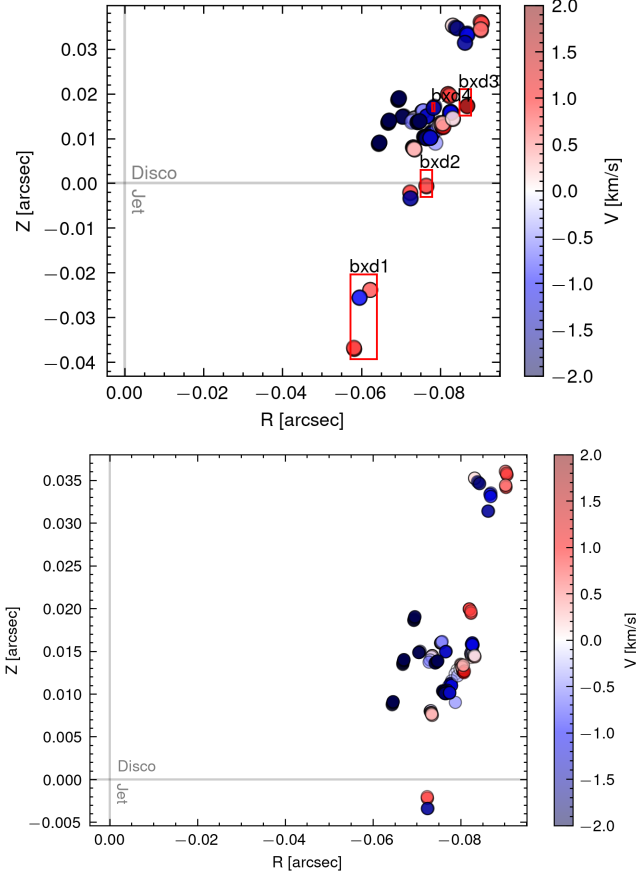
FIG. 11.— Regions to ignore (up), marked in red, (bottom) the finalized map with the sources that will be analyzed.

gular velocity of these traces, that is, we will use the relationship:

$$v = \omega R + v_0 \tag{24}$$

Where v is the measured velocity, ω is the angular velocity, R the distance from the star along the disk coordinate and finally v_0 is a remainder of the velocity, that is the velocity of the entire trace. The angular velocity that we get will have the units of $[km \cdot s^{-1} AU^{-1}]$. Once we calculated ω, it is time to calculate the launch radius the gas traced by the masers, then we must relate the tangential velocity and the velocity given by the Kepler's Laws, which has the form:

$$v = \sqrt{\frac{GM}{R_K}} \tag{25}$$

In this part we must assume that the angular momentum is conserved, and as an implication we assume that the gas that has been expelled from the disk retains the angular velocity it had when it was rotating in the disk with a Keplerian velocity at a radius R_K. About the mass to be used, we will use the values reported by Plunkett et al. (2015), that is $M = 0.43 M_{SUN}$.

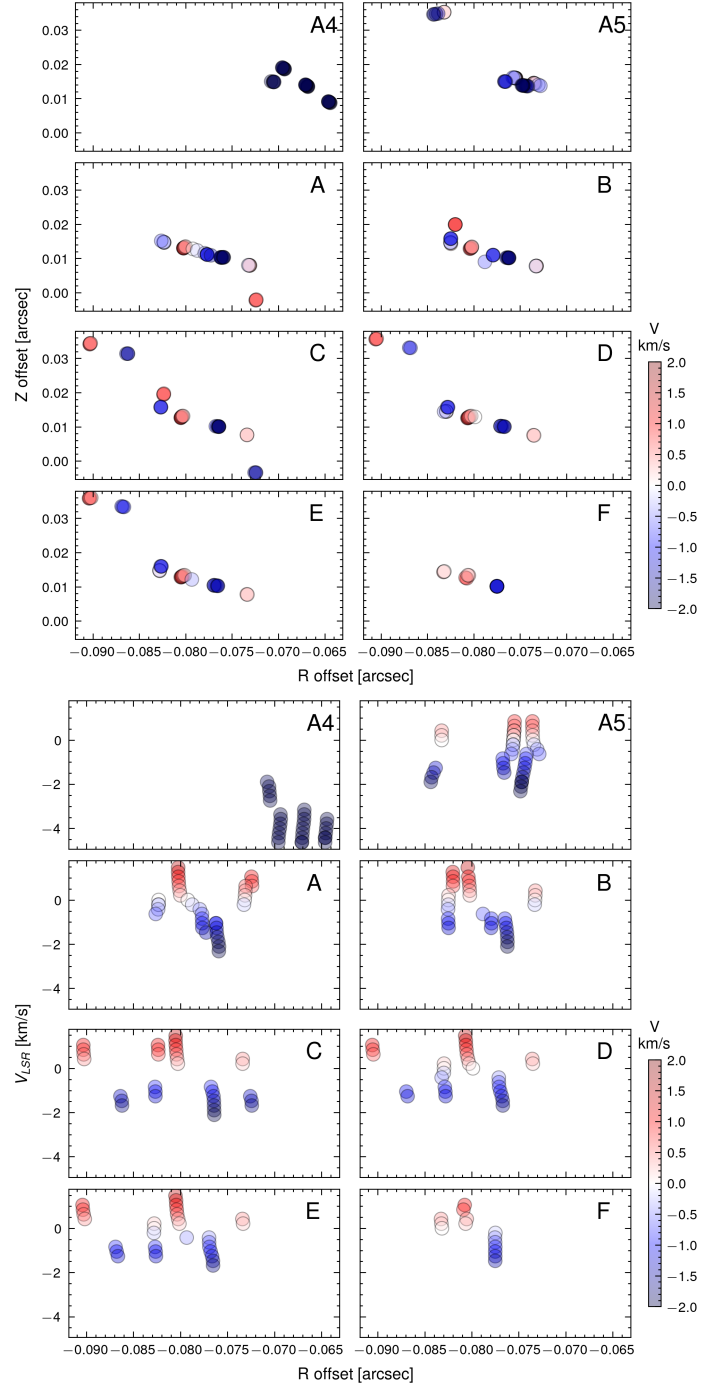Combining the values (and getting rid of v_0), and

FIG. 12.— (up) Spatial distribution of masers by epoch. (bottom) Velocity and distance distribution in R

solving for R_K we obtain:

$$R_K = \sqrt[3]{\frac{GM}{\omega^2}} \tag{26}$$

3.1.2. *Analysis by regions*

From the figure 13 we can recognize certain structures, which we can analyze below:
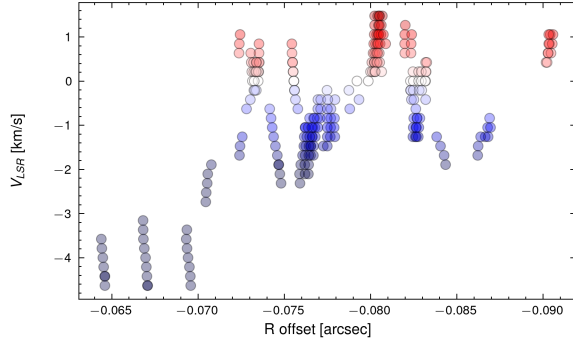
REGION 1

FIG. 13.— Distance from the center of the masers against tangential velocity, structures and gradients are noted.

Region 1 is composed of the following structure (figure 14), we can see that this epoch consists of many points, since these appear in most of the analyzed epochs.
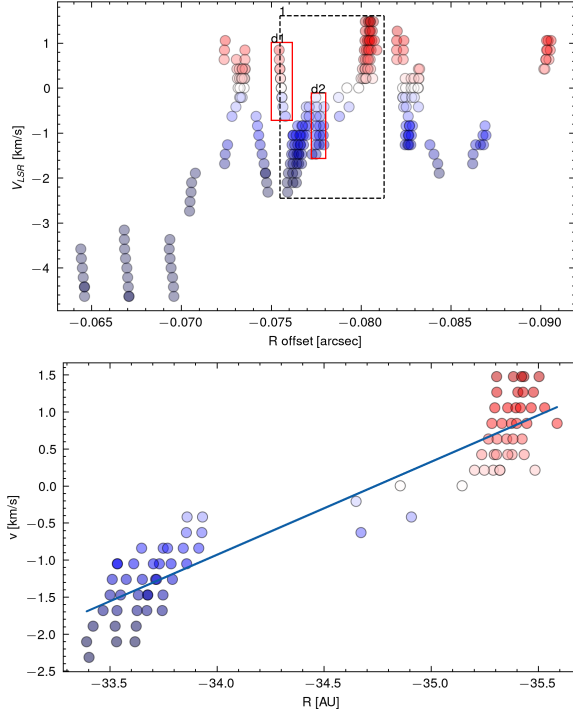

FIG. 14.— Region 1. (Above) The red boxes will be ignored as they belong to another structure. (Bottom) Linear fit of the region

REGION 2

Region 2 (figure 15) is located a little further from the star, around 38 AU, and consists of fewer points.

REGION 3

Region 3 (figure 16) is close to the structure of region 1, it consists of fewer points and that will cause some uncertainty in the regression.

REGION 4

The region is a somewhat hidden structure, very close to region 1 (figure 17).

3.1.3. *Summary of CARMA 6*

Once the linear regression has been carried out, we can obtain the angular velocity of each trace. In ta-
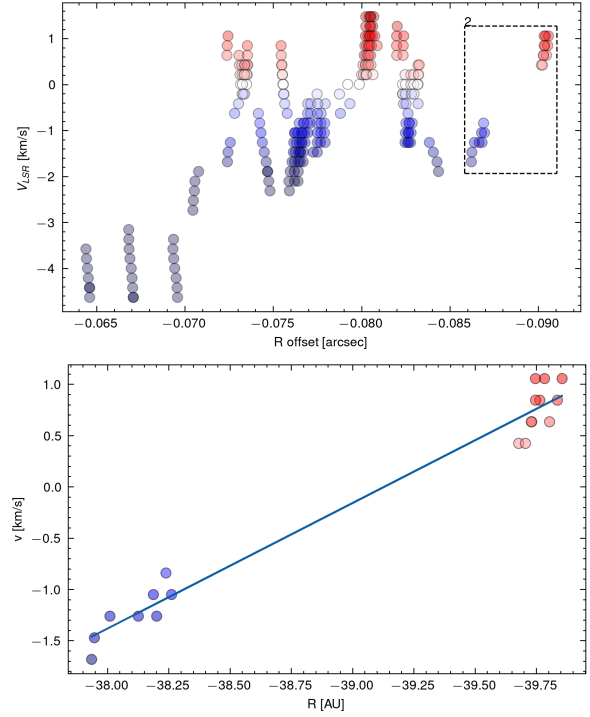

FIG. 15.— Region 2. (Up) The red boxes will be ignored as they belong to another structure. (Bottom) Linear fit of the region
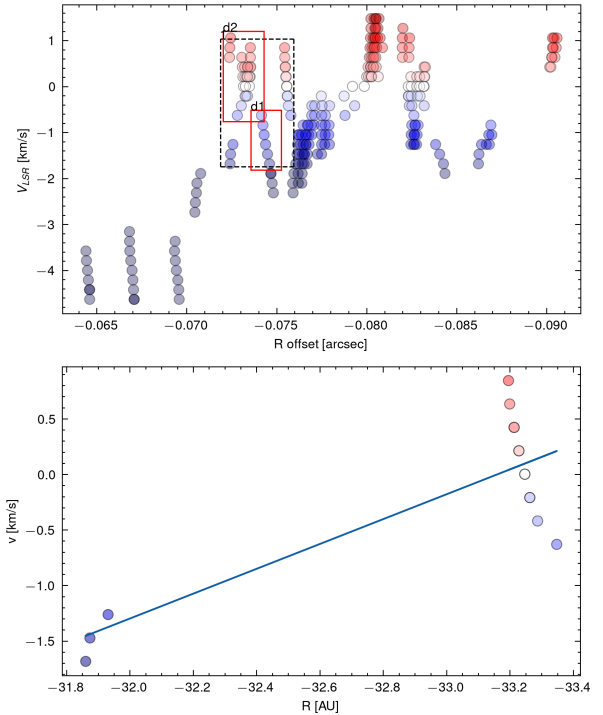

FIG. 16.— Region 3. (Up) The red boxes will be ignored as they belong to another structure. (Bottom) Linear fit of the region

ble 2 we can see the results of the regressions, where the regression has the form $y = ax + b$, and we see that all regions have a Pearson coefficient (R^2) quite acceptable, while the standard deviations of both parameters are relatively small.
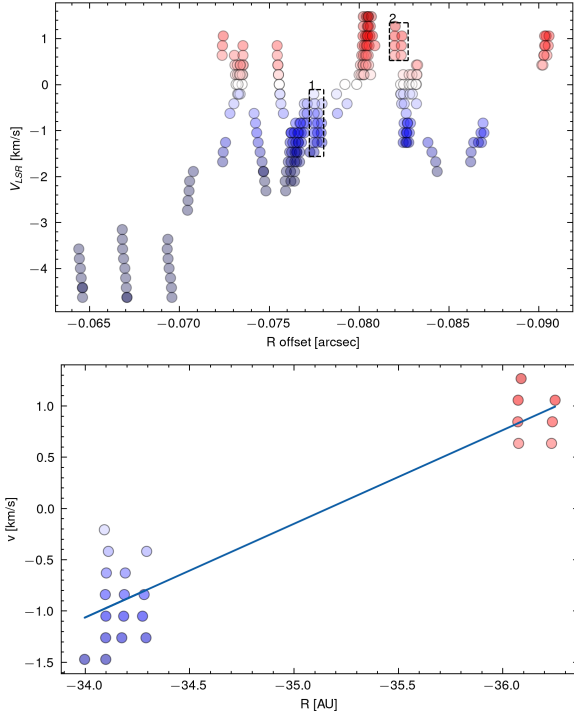
Now, as discussed in the disk velocity section, we

FIG. 17.— Region 4. (Up) Selected regions. (Bottom) Linear fit of the region

TABLE 2
LINEAR REGRESSION RESULTS

Region	a	b	R^2	Δa	Δb
1	-1.2563	-43.6451	0.888	1.712	0.050
2	-1.2242	-47.9014	0.972	0.05	1.961
3	-1.1188	-37.1011	0.680	0.213	7.021
4	-0.9136	-32.1264	0.863	0.080	2.765

TABLE 3
RESULTS OF ANGULAR VELOCITY (ω) AND LAUNCH RADIUS R_K

Region	ω [km $s^{-1} AU^{-1}$]	R_K [AU]
1	≥ -1.2563	≤ 6.1315
2	≥ -1.2242	≤ 6.2384
3	≥ -1.1188	≤ 6.6239
4	≥ -0.9136	≤ 7.5822

can relate the regression to the form of 24, so we recognize that the parameter a of the regression is the angular velocity. Finally, using the relationship 26 we can obtain the launching radius, displayed in table 2.

Why are values limits? This is because the observations assume that the disk-jet system has an angle of 0 between the jet and the plane of the sky, if this would not be true then the angular velocity values would be greater, and the launch radius would be less than the value current. On the other hand, the fact that we have negative values for the angular velocity (ω) indicates that the rotation is clockwise in the plane of the sky .

The launch radii found in the 4 regions can be compared with the literature, mainly with Moscadelli et al. (2022). In this work the authors find larger
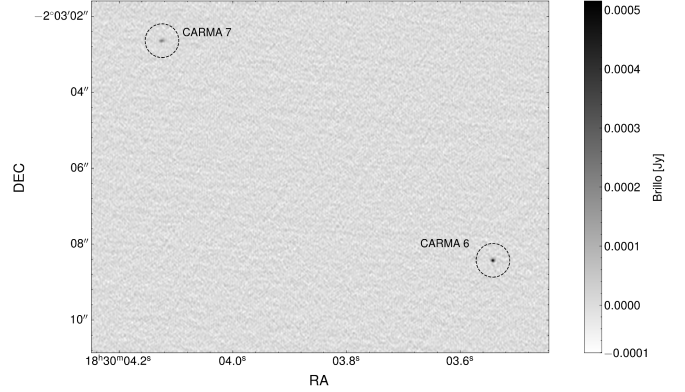

FIG. 18.— Position of CARMA 7 (upper left) and CARMA 6 (lower right) seen on the map obtained with the VLA.
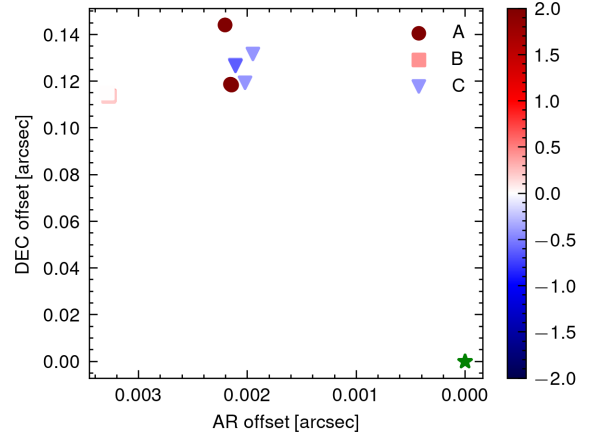

FIG. 19.— CARMA 7 maser map, as can be seen, there are not enough maser observations to carry out an analysis similar to CARMA 6.

launch radii, in the order of 6 to 54 astronomical units, however, it is worth remembering that in the aforementioned article the star studied is of greater mass (approximately 5 solar masses). This can be interpreted as the masers in less massive stars being launched from regions closer to the core. In massive stars the launch radius can also be small (in the same order), but more regions with larger radii were found.

3.2. *CARMA 7*

Let us not forget that CARMA 7 also has maser emission, but it is very dim, making it difficult to analyze in this case in the same way as CARMA 6. This caused a reduced number of sources to be observed in the resulting map (figure **??**). The position of the star, $\alpha = 18h30m4.15s$ and $\delta = -23'3.42''$, was also obtained from the observation with the VLA (`VLA_OBS`), a complementary map to show both stars is seen in figure 18.

3.3. *Spectrum analysis*

Until now we talked primarily about the position and the frequency at which the masers are measured, however, one way in which we can see how the maser evolves month by month or year by year, is by
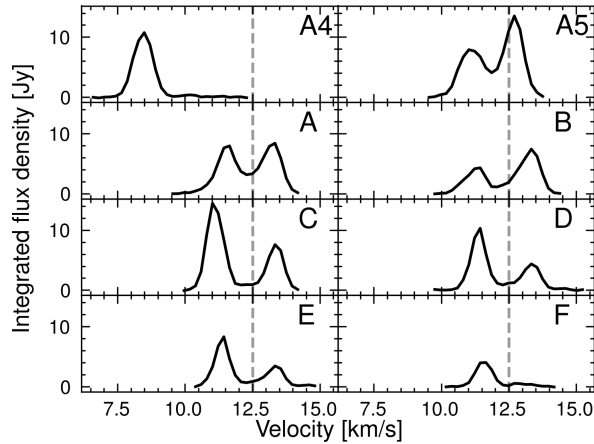
FIG. 20.— Spectrum of the maser emission of all epochs (temporally ordered), the grey line is the rest velocity, it's evident the loss of maser intensity for epoch F.

doing an integration of a region where the masers are located and thus have the flux density (integrated) in Janskys. For this, the CASA `specflux` function was used , which returns the integration of a given region across all channels, and all epochs were plotted together in a matrix shown in figure 20. Something interesting to note is that epoch A4 has few observations, but at the same time the masers are at a frequency far removed from their counterparts from more recent observations. On the other hand, from the A5 epoch onwards it is easy to notice that the maser that was around the star has been losing intensity, that is, it shines less.

4. CONCLUSIONS

Two stars were studied, CARMA 6 and CARMA 7. Both are class 0-I stars, which are located in the South Serpens region (region of high star formation), they have masses of $0.43 M_{sun}$ y $1.21 M_{sun}$ respectively (Plunkett et al. (2015)) . Around both, water masers were observed at 22.2GHz (as reported in Ortiz-León et al. (2021)), the objective of this project was to study the kinematics and spatial distribution of the masers and relate them to a disk wind model.

For this, observational data from the VLBA array (Very Long Baseline Array) were used, they were taken over the course of 2020 to 2022, with a majority of epochs observed in 2022 (monthly data), adding a total of 8 observations for CARMA 6, 3 for CARMA 7, and a complementary observation in 2023 to determine the positions of both stars using the VLA array. These observations have angular resolutions in the order of 1E-4 [arcsec], allowing observations very close to the star. This information is condensed in the table 1.

Using several tools, for example: AIPS (Astronomical Image Processing System) for the calibration of interferometer data, CASA (Common Astronomy Software Applications) for image processing and source analysis, and complementing with codes written in Python, we were able to generate source maps for CARMA 6 and CARMA 7, the latter did not have enough sources, so subsequent steps were not continued.

With CARMA 6, the analysis of traces was carried out, which are coherent structures both spatially and in speed (the latter obtained from the Doppler effect). These structures trace the kinematics of the gas in the vicinity of the star. Furthermore, these sets of traces are consistent with the disk wind model, since their linear spatial distribution and velocity gradients indicate that the gas emerges from the disk surface while maintaining rotation around the star, Al applying a Keplerian model for the disk and conservation of angular momentum, they give us launch radii comparable with specialized literature (Moscadelli et al. (2022)). The radii obtained are around 6 [UA], the rest of the information is compiled in table 2.

Thus, it can be concluded that this project provides new observational evidence that supports the disk wind model as a mechanism for the star to release angular momentum, through the production of protostellar jets. On the other hand, it remains a future perspective to analyze with new observations whether the masers can present a periodicity, that is, in some years we do not see them and later they are observed again. Finally, this project was a great learning experience in radio astronomy tools, interferometer calibration and astronomical data processing in general.

ACKNOWLEDGEMENTS

REFERENCES

Anglada, G., Rodriguez, L. F., & Carrasco-Gonzalez, C. 2018, The Astronomy and Astrophysics Review, 26, 3

Dunham, M. M., Stutz, A. M., Allen, L. E., Evans, N. J., Fischer, W. J., Megeath, T., Myers, P. C., Offner, S. S. R., Poteet, C. A., Tobin, J. J., & Vorobyov, E. I. 2014, University of Arizona Press eBooks

Gray, M. 1999, Philosophical Transactions of the Royal Society of London. Series A: Mathematical, Physical and Engineering Sciences, 357, 3277

Kettenis, M., van Langevelde, H. J., Reynolds, C., & Cotton, B. 2006, NASA ADS, 351, 497

Lee, C.-F. 2020, The Astronomy and Astrophysics Review, 28

Loinard, L., Torres, R. M., Mioduszewski, A. J., Rodriguez, L. F., Gonzalez-Lopezlira, R. A., Lachaume, R., Vazquez, V., & Gonzalez, E. 2007, The Astrophysical Journal, 671, 546

Moscadelli, L., Sanna, A., Beuther, H., Oliva, G. A., & Kuiper, R. 2022, nature astronomy, 6, 1068

Ortiz-León, G. N., Plunkett, A., Loinard, L., Dzib, S. A., Rodríguez-Garza, C. B., Pillai, T., Gong, Y., & Brunthaler, A. 2021, The Astronomical Journal, 162, 68

Plunkett, A. L., Arce, H. G., Corder, S. A., Dunham, M. M., Garay, G., & Mardones, D. 2015, The Astrophysical Journal, 803, 22

Podio, L., Tabone, B., Codella, C., Gueth, F., Maury, A., Cabrit, S., Lefloch, B., Maret, S., Belloche, A., André, P., Anderl, S., Gaudel, M., & Testi, L. 2021, Astronomy and Astrophysics, 648, A45

Reid, M. J., Menten, K. M., Brunthaler, A., Zheng, X. W., Dame, T. M., Xu, Y., Wu, Y., Zhang, B., Sanna, A., Sato, M., Hachisuka, K., Choi, Y. K., Immer, K., Moscadelli, L., Rygl, K. L. J., & Bartkiewicz, A. 2014, The Astrophysical Journal, 783, 130

Richer, J. & Padman, R. 1991, Monthly Notices of the Royal Astronomical Society, 251, 707

Thompson, A. R., Moran, J. M., & Swenson, G. W. 2017, Interferometry and Synthesis in Radio Astronomy (Springer International Publishing)

Wilson, T. L., Rohlfs, K., & Huttemeister, S. 2016, Tools of radio astronomy (Springer)